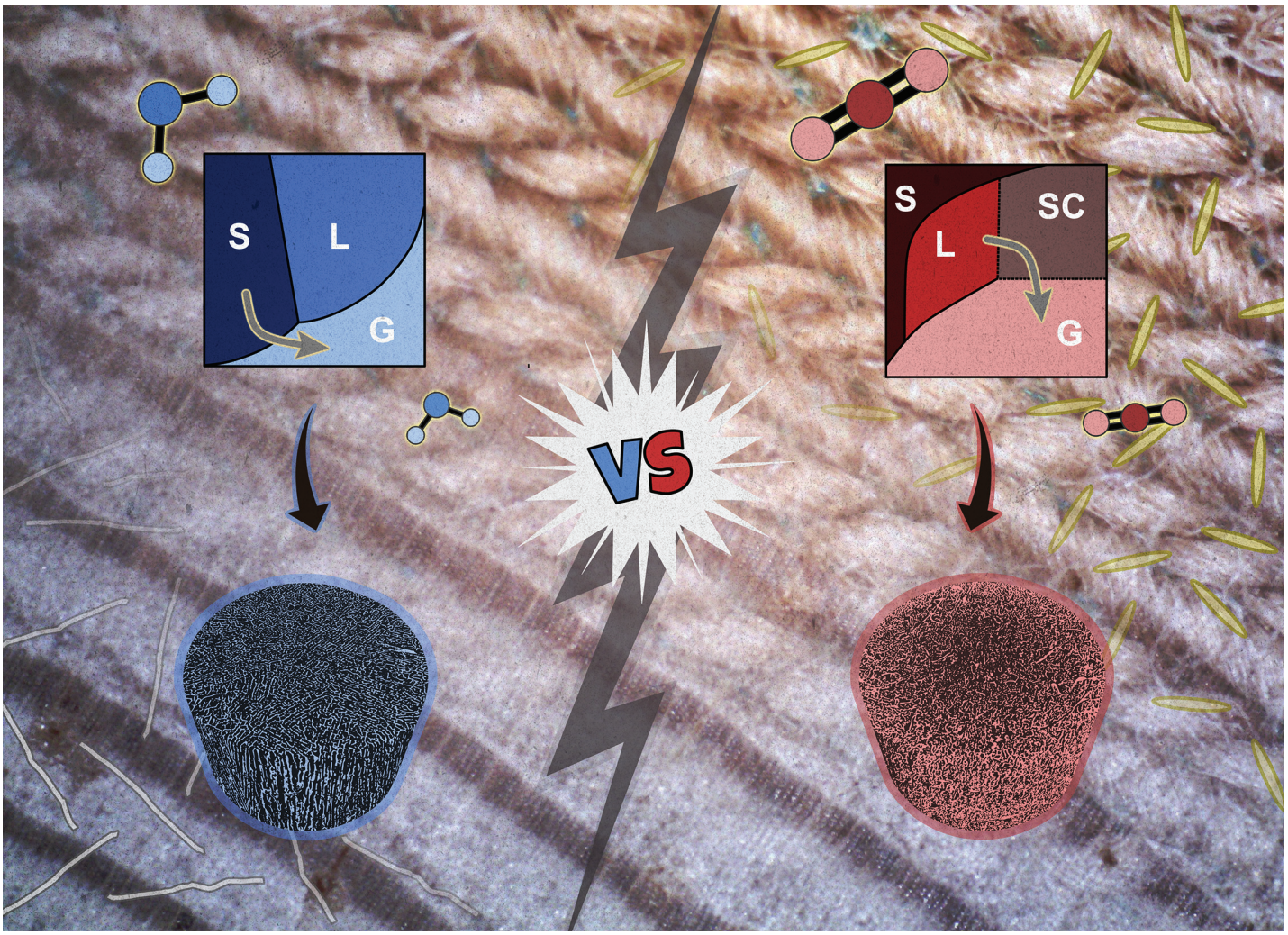

Showcasing research from Dr. Varvara Apostolopoulou-Kalkavoura, Professor Lennart Bergström and Dr. Gustav Nyström, from Stockholm University and Empa from Sweden and Switzerland.

The influence of drying routes on the properties of anisotropic all-cellulose composite foams from post-consumer cotton clothing

Cellulose nanomaterials from post-consumer cotton textiles and wood were used to create foams *via* freeze drying (FD) and supercritical drying (SCD). Despite identical compositions, FD and SCD foams exhibited different structural, thermal, mechanical and moisture resilience properties due to nanoparticle orientation and foam wall structure. The SCD foams were better adsorbents and the FD foams were suitable for load-bearing applications while both maintained good insulation capacity.

As featured in:

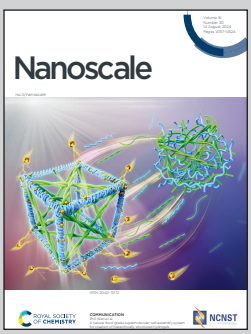

See Gustav Nyström, Lennart Bergström, Varvara Apostolopoulou-Kalkavoura *et al.*, *Nanoscale*, 2024, **16**, 14275.

ROYAL SOCIETY OF CHEMISTRY

rsc.li/nanoscale

Registered charity number: 207890

Nanoscale

ROYAL SOCIETY OF CHEMISTRY

PAPER

View Article Online
View Journal | View Issue

Cite this: *Nanoscale*, 2024, **16**, 14275

The influence of drying routes on the properties of anisotropic all-cellulose composite foams from post-consumer cotton clothing†

Carina Schiele, [a] Maria-Ximena Ruiz-Caldas, [a] Tingting Wu,[b,c] Elisabetta Nocerino,[a,d] Agnes Åhl, [a] Aji P. Mathew, [a] Gustav Nyström, *[b] Lennart Bergström *[a,e] and Varvara Apostolopoulou-Kalkavoura *[a,b]

Biopolymer-based functional materials are essential for reducing the carbon footprint and providing high-quality lightweight materials suitable for packaging and thermal insulation. Here, cellulose nanocrystals (CNCs) were efficiently upcycled from post-consumer cotton clothing by TEMPO-mediated oxidation and HCl hydrolysis with a yield of 62% and combined with wood cellulose nanofibrils (CNFs) to produce anisotropic foams by unidirectional freeze-casting followed by freeze drying (FD) or supercritical-drying (SCD). Unidirectional freeze-casting resulted in foams with aligned macropores irrespective of the drying method, but the particle packing in the foam wall was significantly affected by how the ice was removed. The FD foams showed tightly packed and aligned CNC and CNF particles while the SCD foams displayed a more network-like structure in the foam walls. The SCD compared to FD foams had more pores smaller than 300 nm and higher specific surface area but they were more susceptible to moisture-induced shrinkage, especially at relative humidities (RH) > 50%. The FD and SCD foams displayed low radial thermal conductivity, and the FD foams displayed a higher mechanical strength and stiffness in compression in the direction of the aligned particles. Better understanding how drying influences the structural, thermal, mechanical and moisture-related properties of foams based on repurposed cotton is important for the development of sustainable nanostructured materials for various applications.

Received 19th April 2024,
Accepted 27th June 2024

DOI: 10.1039/d4nr01720j

rsc.li/nanoscale

Introduction

The design of safe and functional materials from renewable feedstocks for high-performance is a key challenge. As a non-toxic, biodegradable and highly abundant material, cellulose is a strong candidate for such endeavors. Cellulose nanomaterials (CNMs) extracted from wood have been assembled into functional and bio-based materials such as films, coatings, beads, capsules, continuous fibers, hydrogels, cushioning materials, foams and aerogels.[1,2] There is a growing interest to replace or reduce the use of virgin resources (*i.e.* wood) and instead extract CNMs from post-consumer clothing, *e.g.* in the form of cellulose nanocrystals (CNCs).[3] Using post-consumer clothing as a CNM source can increase the sustainability of CNM extraction,[4] and also partly mitigate the growing problem of textile waste.[5]

Assembling upcycled textile fibers into functional and lightweight materials such as packaging and insulation materials that can replace fossil-based materials can also reduce the carbon footprint. However, it is essential that the biobased and upcycled foams display mechanical robustness, high moisture resilience and a low thermal conductivity. In porous materials like foams and aerogels, the thermal conductivity is mostly determined by the heat transfer *via* gas and solid conduction.[6] Both modes can be influenced by the composition, density and structure of the material with the pore size playing a major role on the gas conduction and the type of bonds and interfaces in the solid part determining the solid conduction.[7–10]

The ability to attract and hold water plays an important part in the moisture resilience of a material and is especially important for materials based on cellulose which is a well-known

[a]*Department of Materials and Environmental Chemistry, Stockholm University, SE-10691 Stockholm, Sweden. E-mail: lennart.bergstrom@mmk.su.se, varvara.apostolopoulou@mmk.su.se*
[b]*Cellulose & Wood Materials Laboratory, Empa, Überlandstrasse 129, CH-8600 Dübendorf, Switzerland. E-mail: gustav.nystroem@empa.ch*
[c]*Institute of Sustainability for Chemicals, Energy and Environment (ISCE2), Agency for Science, Technology and Research (A*STAR), 1 Pesek Road, Jurong Island 627833, Singapore*
[d]*Laboratory for Neutron Scattering and Imaging, Paul Scherrer Institute (PSI), Villigen, CH-5232, Switzerland*
[e]*Wallenberg Initiative Materials Science for Sustainability, Department of Materials and Environmental Chemistry, Stockholm University, 114 18 Stockholm, Sweden*
† Electronic supplementary information (ESI) available. See DOI: https://doi.org/10.1039/d4nr01720j

hygroscopic material. The composition and functional groups of a material as well as its particular structure have a big influence on its interaction with moisture.[11,12]

The mechanical robustness and load-bearing ability of a material is determined by the strength of the chemical bonds present in it as well as the occurrence of defects and dislocations in the alignment of the material.[13]

Foams prepared by unidirectional freeze-casting, under a temperature gradient result in highly anisotropic structures, typically featuring aligned columnar macropores.[14,15] Ambient drying is the most sustainable drying technique[16] but susceptible to drying-induced shrinkage and deformations. Freeze drying (FD) and supercritical drying (SCD) are known to avoid capillary forces and therefore prevent shrinkage and keep structural integrity.[17,18] While studies on isotropic polysaccharide-based porous materials prepared *via* supercritical drying revealed smaller pore sizes and a larger surface area than porous materials with the same composition prepared *via* freeze drying,[19–21] studies on anisotropic materials are sparse.[15] Previous studies confirmed that anisotropic CNF-based foams can be prepared following both drying strategies by applying unidirectional ice-templating prior to drying which result in foams with aligned macropores due to the large ice-crystals.[15,22,23] Anisotropic cotton CNC-based foams have also been prepared by freeze-casting and freeze drying.[18]

In this study, we prepared anisotropic composite foams from upcycled post-consumer cotton CNCs and wood-derived CNFs with different densities by unidirectional freeze-casting and subsequent drying. The effect of freeze drying and supercritical drying on the structural features such as pore size, alignment and surface area of the foams were connected to the thermal conductivity, mechanical properties and moisture resilience.

The FD foams displayed higher macropore alignment, bigger pore sizes, lower surface area and a higher moisture resilience than the SCD foams. The nanoparticles inside the foam wall were aligned for the FD foams but not for the SCD foams that correlated well with the higher Young's Modulus and toughness, and lower radial thermal conductivity of the FD foams.

Experimental section

Materials

Sorted and clean post-consumer cotton clothing was provided by Wargön Innovation, primarily consisting of dyed T-shirts and other tops based on visual assessment. Never-dried sulfite softwood cellulose pulp (Domsjö dissolving Plus) was provided by Domsjö Fabriker AB (Aditya Birla Domsjö, Sweden). Sodium hypochlorite (NaClO, 6–14% Fisher Scientific), 2,2,6,6-tetramethyl-1-piperidinyloxy free radical (TEMPO, ≥98%, Alfa Aesar), standardized sodium hydroxide (NaOH, 0.1 M Fisher Chemical™), sodium hydroxide pellets (NaOH, >98% Honeywell Fluka™), sodium bromide (NaBr, BioUltra, P99.5%, Sigma Aldrich), hydrochloric acid (HCl, 37 wt% AnalaR® Normapur®) were used as received. Deionized (DI) water was used for all solutions and dispersions.

Extraction of CNCs and CNFs

The post-consumer cotton clothing was cut into ~1 cm^2 pieces using a paper guillotine. No pretreatment was performed prior to the TEMPO-oxidation. The cotton derived TEMPO-oxidized cellulose nanocrystals (CNCs) were prepared by TEMPO-mediated oxidation followed by HCl hydrolysis as described in our previous work.[18] In brief, square pieces of cotton were oxidized with NaClO using TEMPO/NaBr as a catalyst/co-catalyst system. NaClO was added dropwise, maintaining the pH above 10 with 1 M NaOH. After four hours, the mixture was vacuum-filtered through a 5 μm nylon mesh and rinsed with deionized water. The oxidized cotton was then hydrolyzed with 4 M HCl at 80 °C for four hours, followed by cooling in an ice bath. The suspension was cleaned by centrifugation (Sorvall LYNX 6000, Thermo Scientific, USA) for 10 min and 24 000*g* (11 880 rpm). Further, the sediment was dialyzed for about 8–10 days until the conductivity of the dialysis water was below 2 μS cm^{-1} for two consecutive days. The clean dispersion was immersed in an ice bath and sonicated at 60% of amplitude with an on/off pulse of 2 s for 10 min using an ultrasonic homogenizer (500 W, 20 kHz, Q500, Qsonica). The CNCs were neutralized with NaOH until reaching a pH of 7.8. The starting CNC dispersion was concentrated to 9 wt% using a rotary evaporator at 60 °C under vacuum. The CNC yield was calculated from the dry mass recovered after the TEMPO-mediated oxidation and the HCl hydrolysis. The yield was calculated according to the following equation with the reported value being the average of three batches:

$$\frac{\text{dry mass of CNC [g]}}{\text{dry mass of cotton [g]}} \quad (1)$$

The wood derived TEMPO-oxidized cellulose nanocrystals (CNCs) were prepared by TEMPO-mediated oxidation followed by mechanical defibrillation as described previously.[22]

Preparation of anisotropic foams

Composite CNC and CNF anisotropic foams with varying densities were prepared by ice-templating. The composite CNC and CNF foams were prepared from 1, 3 and 5 wt% dispersions in 1 : 1, 5 : 1 and 9 : 1 CNC : CNF mass ratios respectively. The dispersions of CNMs were ice-templated in molds with copper bottoms and Teflon walls placed on a copper block immersed in liquid nitrogen ensuring unidirectional freezing from the bottom to the top. Two different mold sizes (1.5 × 2.0 cm and 4.0 × 2.5 cm) were used, adding 5 and 30 g of dispersions, respectively.

The frozen dispersions were dried by two different routes: FD and SCD. The anisotropic FD foams were obtained through ice sublimation at −60 °C and 0.024 mbar over four days, using a freeze dryer (Christ Alpha 1-2LDplus, Germany). Prior to the SCD, the unidirectionally frozen dispersions were placed in 99.9% ethanol solution to allow the solvent exchange from

water to ethanol due to its miscibility with carbon dioxide used for the supercritical drying. In order to achieve an ethanol content of >99.5% in the alcogels, the solvent exchange using fresh ethanol had to be repeated 4 times. The exchanged alcogels were then supercritically dried using the Separex Supercritical Fluid Technology (France). The first step of SCD process was the pressurization to reach 120 bar and 45–47 °C which lasted 45 min. The main step was the drying, performed at 120 bar and 45–47 °C and lasted 5–10 h depending on the number of samples loaded. The last step included 1 h depressurization. There was shrinkage observed after the supercritical drying which is estimated to be about 39%, 46%, 66% for CNC : CNF_9 : 1_SCD, CNC : CNF_5 : 1_SCD and CNC : CNF_1 : 1_SCD, respectively and 19%, 26%, 32% for the freeze dried foams CNC : CNF_9 : 1_FD, CNC : CNF_5 : 1_FD and CNC : CNF_1 : 1_FD, respectively.

Characterization

Atomic force microscopy (AFM). The morphology of the CNMs was evaluated by imaging with a Multimode-8 atomic force microscope (Bruker, USA) in peak-force tapping mode with the ScanAsyst™ algorithm using ScanAsyst™ tips. The dispersions of CNMs were diluted to 0.001 wt% prior to the imaging and one drop was placed onto freshly cleaved mica and dried at room temperature.

Conductometric titration. CNC and CNF dispersions with a concentration of 0.25 wt% and 0.05 wt%, respectively, were prepared for the titrations in 100 ml aqueous solution. To reach a pH below 2.5 to ensure the protonation of all the available carboxyl groups, 110 μL of 5 M HCl was added to the dispersions. The dispersions were titrated using 0.1 M NaOH (Titripur®) as titrant and the conductivity was recorded every 30 seconds after adding 0.05–0.2 ml of the titrant until reaching pH = 11. The charge density was estimated from the volume of NaOH consumed in the flat region, corresponding to the neutralization of the carboxyl groups, and from the linear regressions in the 3 regions of the conductivity against volume of NaOH curve. The value reported are averaged after of two to four conductometric titrations.

Scanning electron microscopy (SEM). The radial and axial directions of both the FD and SCD anisotropic foams were assessed by SEM imaging using a HITACHI TM-3000 (Japan) using a 15 kV electron beam at a magnification of 300. The FD foam fragments were obtained by cryo-cutting while the SCD foam fragments were obtained by cutting the dried foams with a sharp blade. The high resolution SEM images were recorded on a JEOL JSM IT-800 (Japan) using a 15 kV electron beam at a magnification of 500 and 40 000. The samples were prepared by peeling off a layer of a dried foam wall layer with a sticky carbon tape on the sample holder and coating with Au particles using a gold sputter JFC 1200 fine coater (Japan), operating at 10 mA for 60 seconds, yielding particles in the size range 5 to 15 nm.

The degree of orientation of the columnar macropores was assessed using the "OrientationJ" plugin of Fiji. It compared the orientation angle of a pixel with respect to its neighboring pixel. The resulting histograms of the frequency plotted against the orientation angle, were then fitted to a Gaussian curve and the full width half maximum (fwhm) of the curve was derived. The fwhm was then used to determine the orientation degree following eqn (2).

$$f = \frac{180 - \text{fwhm}}{180} \quad (2)$$

Nitrogen and carbon dioxide sorption. Nitrogen adsorption was performed to estimate the specific surface area and the pore volume of all foam configurations using an ASAP 2020 Plus Adsorption Analyzer (Micromeritics Instrument Corporation, Nocross, GA, United States). Foam samples of approximately 0.6–1 g, depending on the density, were degassed at 70 °C for 14 h. The specific surface area and the pore volume were then calculated based on the BET and BJH methods, respectively.

The SCD samples were also tested for CO_2 adsorption at 0 °C and 1 atm following the same protocol for the degassing. The CO_2 adsorption was repeated 5 consecutive times for each sample.

Mechanical compression. The Young's modulus and the toughness of the FD and SCD foams along the freezing direction were calculated from the stress–strain curve of compression tests at 23 °C and 50% RH using an Instron 5944 mechanical testing instrument (Instron, USA) equipped with 100 N and 1000 N load cells. The foams were conditioned for 48 h at 23 °C and 50% RH prior to the compression tests. The compression measurements were repeated for at least five specimens from each foam configuration at a compression rate of 1 mm min^{-1}. The Young's modulus was calculated from the slope of the linear region of the stress–strain curve, and the toughness was calculated from the area under the stress–strain curve up to 70% strain.

Moisture uptake. The moisture uptake of the FD and SCD foams was measured by an analytical balance (BCE224-1S, Sartorius, Germany) placed inside a temperature- and humidity-controlled chamber (EVO, Climacell, USA). The balance was connected to a computer recording the mass every 300s. The moisture content was measured as a function of RH (10, 20, 35, 50, 65 and 80%) at 295 K and a measurement time of 6 h. The dry condition was estimated by drying in an oven (Binder, Germany) at 105 °C and determining the weight loss after drying until constant weight.

Shrinkage. The moisture dependent shrinkage was determined by placing one foam of each configuration in a vessel connected to a humidifier. The volume was measured as a function of RH (20, 35, 50, 65 and 80%) at 295 K after two hours of exposure (unless specified differently) using a caliper.

Thermal conductivity. The thermal conductivities of all foam configurations in the radial and axial direction were measured using the TPS 2500 S Hot Disk Thermal Constants Analyzer in the anisotropic mode. Two identical foams were used for each measurement. The transient plane sensor with a radius of 6.4 mm was placed between the two foam pieces and a small weight was added on the top to ensure a tight place-

ment and good thermal contact between the sensor and the foams. The heating power and the measurement time were 10 mW and 10 s (CNC : CNF-1 : 1:FD) 10 mW and 20s (CNC : CNF-1 : 1:SCD), 10 mW and 40s (CNC : CNF-5 : 1:FD, CNC : CNF-5 : 1:SCD, CNC : CNF-9 : 1:SCD), 15 mW and 40s (CNC : CNF-5 : 1:FD,) respectively. The measurements were conducted at 295 K and 7, 20, 35, 50, 65 and 80% RH in a customized cell as described before.[24] The radial thermal diffusivity and conductivity were determined using the volumetric specific heat capacity of the foams at the specific RH as input information. The latter was derived from the specific heat capacity (Cp) of the wet solid material (Cp_{wet}) derived from eqn (3) multiplied with the density of the wet foam derived from eqn (4).

$$Cp_{wet} = (1 - H_2O_w) \times Cp_{dry} + Cp_{H_2O} \times H_2O_w \quad (3)$$

$$\rho_{wet} = \frac{m_{dry} + m_{H_2O}}{V_{dry} \times \text{shrink\%}} \quad (4)$$

Here H_2O_w is the wt% of water at a certain RH derived from the moisture uptake experiments, Cp_{H_2O} is the Cp of water (4181 J kg^{-1} K^{-1}) and Cp_{dry} is the Cp of the dry solid. Isotropic reference samples were prepared *via* crash freezing in liquid nitrogen and measured with the isotropic mode of the Hot Disk to determine the volumetric Cp of the isotropic reference sample which was divided by its density to derive Cp_{dry}. Furthermore is m_{dry} the mass of the dry foam, m_{H_2O} the mass of water adsorbed on the foam, V_{dry} the volume of the dry foam and shrink% the percentage of volume shrinkage. The axial thermal diffusivity and conductivity were obtained using the software provided by Hot Disk. The error bars of the thermal conductivity measurements represent the sample standard deviation of n = 15. The super-insulating reference material (polyurethane aerogel) was purchased from the Center of Applied Energy Research e.V.[25,26]

Powder X-ray diffraction (PXRD). PXRD data of both samples (CNCs and CNFs) were collected on a Panalytical X'Pert Pro diffractometer (Cu Kα1,2, l1 = 1.540598 Å, l2 = 1.544426 Å) set up in a Bragg–Brentano geometry and operated at 45 kV and 40 mA. The measurements were performed over pellets (200 mg) made of frze-dried CNCs and CNFs on zero-background SI plates. The deconvolution of each diffractogram was carried by fitting each peak to a Voigt function using the Fityk peak-fitting software.

Wide-angle X-ray scattering (WAXS). A Bruker D8 Venture single-crystal diffractometer equipped with a Photon II detector and Cu-Kα radiation (λ = 1.5418 Å) was used at a detector distance of 70 mm and an acquisition time of 180 s. 2D WAXS patterns obtained from uncompressed foam pieces were used to derive the orientation degree *f*. Therefore, the signal of the (200) reflection at 2θ = 22.7° was azimuthally integrated and after background subtraction the curve of the diffraction intensity with respect to the azimuthal angle was fitted to a Gaussian function. The degree of orientation *f* was then calculated from the fwhm of the received curve following eqn (1).

Small angle X-ray scattering (SAXS). SAXS data were collected at Petra III's P62 instrument with a 200 × 200 μm beam size and 12 keV energy. Foams were cut to 2 mm thickness to avoid multiple scattering, with a 1.1 s total exposure time per measurement. The sample-to-detector distance was 7 m, providing a q-range of 0.004–0.14 $Å^{-1}$, using an EIGER2 9M detector. Calibration, integration, averaging, and normalization were performed using the PyFAI library in Python 27. No radiation damage was observed. Relative humidity (RH) between 5% and 80% was controlled *in situ* using a MHG32 generator and a sealed die-cast aluminum box. Samples equilibrated for 30 minutes at each RH level. The orientation of nanoparticles was kept perpendicular to the X-ray beam.

To derive the scale factor C, proportional to the specific surface area, the high q region of SAXS 1D patterns (0.07 $Å^{-1}$ < q < 0.14 $Å^{-1}$ for FD foams, 0.10 $Å^{-1}$ < q < 0.14 $Å^{-1}$ for SCD foams) was fitted with the Porod model.[27–29]

$$I(q) = \frac{C}{q^4} + \text{BG} \quad (5)$$

For the orientation degree *f*, the 2D scattering pattern was azimuthally integrated and fitted to a Gaussian curve. The fwhm of the intensity was used to calculate *f*.

Tomographic imaging. X-ray tomography data were collected at MAXIV's ForMAX instrument with a 1 mm × 1 mm field of view, 10x magnification, and 0.65 μm voxel size. Foams were cut to 1 mm x 1 mm to facilitate beam alignment and rotation center identification. Data were acquired through 360-degree rotational scans with 1800 projections (100 ms exposure, 30 ms latency) at 35% and 90% RH, using a Cellkraft P-10 humidifier. Background subtraction was performed using flat- and dark-field images. 3D reconstructions were made using the gridrec algorithm and visualized with Fiji. No phase retrieval or contrast enhancement was applied.

Results and discussion

CNCs from post-consumer cotton clothing (Fig. 1a) and CNFs from wood (Fig. 1b) were used as building blocks for the preparation of anisotropic foams by unidirectional ice-templating (Fig. 2a). Due to the very high cellulose content of cotton clothing (>90%),[30] the processing into CNCs did not require any time- and energy-demanding pretreatment of the clothing. The wood CNFs were extracted from sulfite softwood pulp by TEMPO-mediated oxidation followed by grinding as described in previous work.[22,23] Both cotton CNCs and wood CNFs were extracted using the same chemicals-to-cellulose ratio and had COO^- functional groups on the C6 of cellulose and Na^+ as counter-ion. However, as the crystallite size of cotton and wood differ,[31] the degree of substitution of the C6 is not the same resulting in different surface charges for the two CNMs. Cotton CNCs and wood CNFs had a surface charge of 1142 ± 90 and 1646 ± 28 mmol COO^- per kilogram of cellulose, respectively (Fig. S1a and b†). The surface charge of the oxidized cotton CNCs corresponds well to the highest value

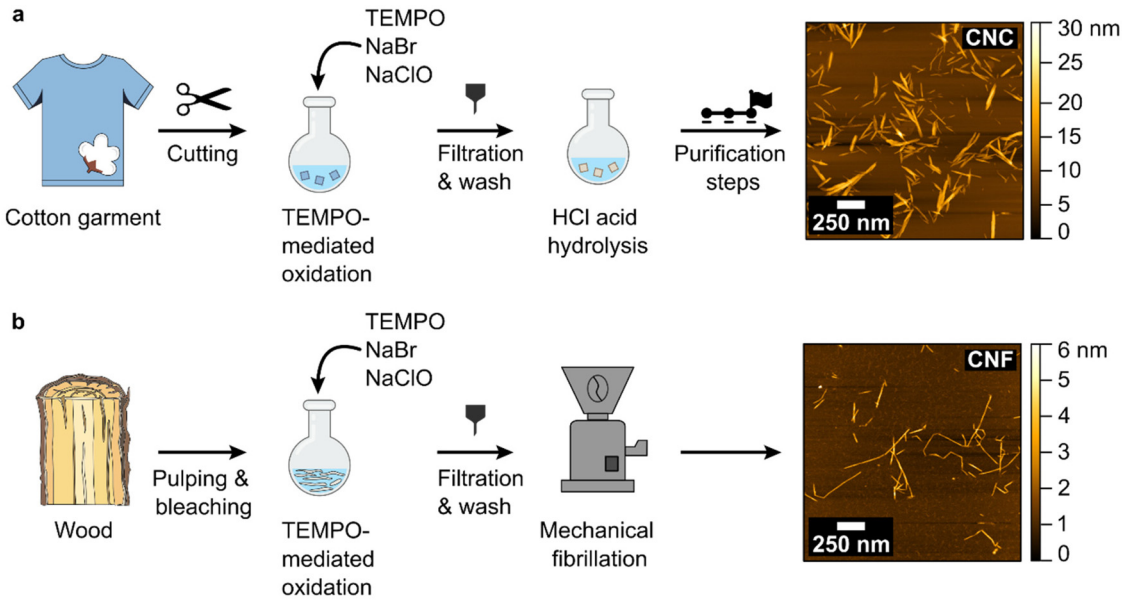

Fig. 1 Schematic illustration of the extraction of cellulose nanomaterials (CNMs). (a) Extraction of cellulose nanocrystals (CNCs) from post-consumer cotton clothing. (b) Extraction of cellulose nanofibrils (CNFs) from wood.

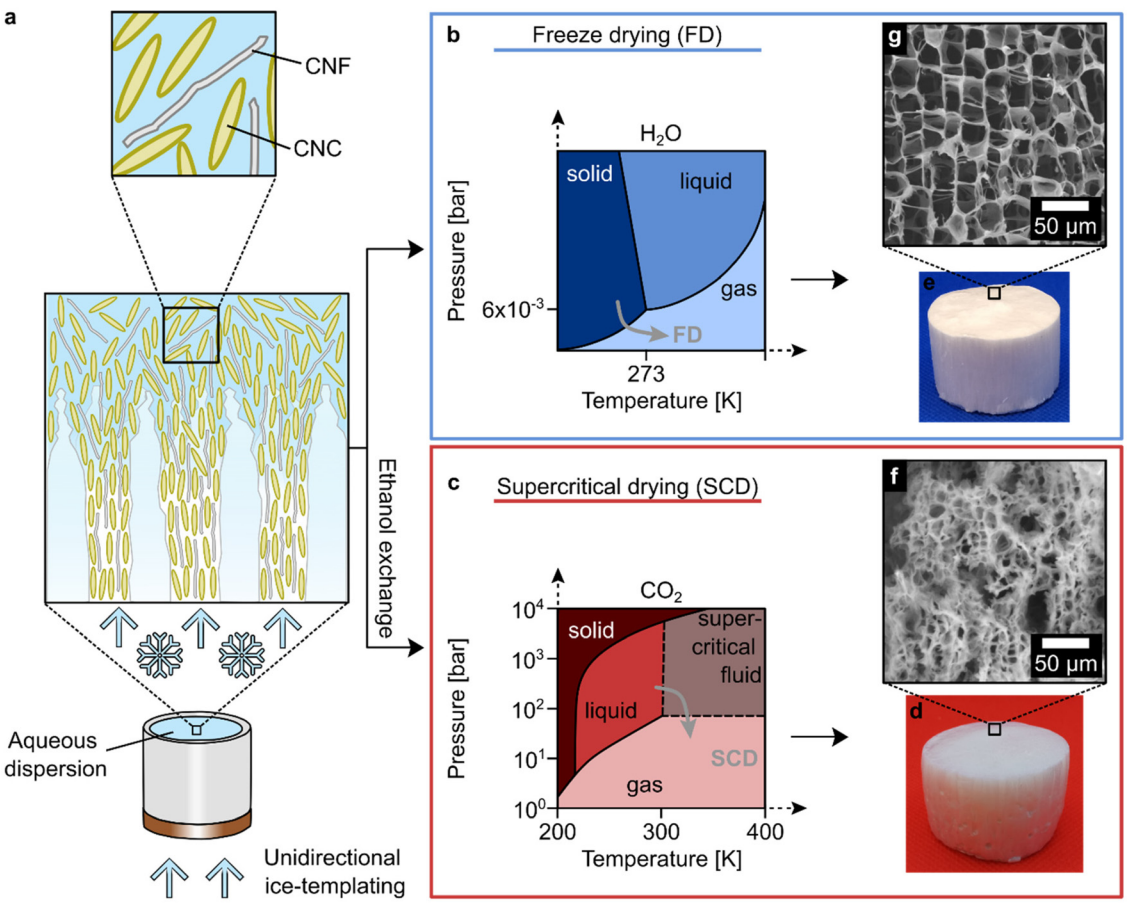

Fig. 2 Preparation of anisotropic CNC–CNF foams. (a) Unidirectional ice-templating of CNC–CNF aqueous dispersions. Preparation of dry CNC–CNF anisotropic foams by (b) freeze drying (FD) and (c) supercritical drying (SCD). (d) (e) Picture and (f) (g) SEM image of the cross-section of CNC : CNF-9 : 1_FD and CNC : CNF-9 : 1_SCD foams, respectively.

reported for functionalization of the C6 of cellulose in cotton.[31] Cotton clothing-derived CNCs exhibited a larger diameter (5.8 ± 2.6 nm) than wood-derived CNFs (2.7 ± 0.9 nm). This difference is attributed to the larger crystallite size of cotton compared to wood pulp[32] (Fig. 1 and Fig. S2†). Conversely, the aspect ratio was smaller for cotton clothing CNCs (29 ± 13) than for wood CNFs (120 ± 91), due to the different preparation methods of acidic hydrolysis and mechanical fibrillation, respectively. Since sodium hypochlorite, a cost-effective bleaching agent,[33] was used as oxidizing agent in the TEMPO-mediated oxidation the dye molecules of the cotton clothing were degraded resulting in CNCs with a light-yellow haze.

Aqueous dispersions of CNCs and CNFs with different solid contents (1 wt%, 3 wt% and 5 wt%) and different CNC : CNF mass ratios (1 : 1, 5 : 1 and 9 : 1) were unidirectional freeze cast (Fig. 2a) and either freeze dried (Fig. 2b) or subjected to ethanol exchange to allow subsequent supercritical drying with CO_2 (Fig. 2c). The CNFs, even at small quantities (0.5 wt% in dispersion), ensured the integrity of the alcogels during the ice-to-ethanol exchange step due to the fibrils' large aspect ratios and entanglements. On the other hand, ice-templated specimens made entirely from CNCs did not result in self-standing alcogels, which can be attributed to the weak network formation at low and intermediate concentrations of the rigid rod-like CNCs. We have investigated the properties and structural features of composite foams of three different compositions (and densities) that were prepared by either FD (Fig. 2d) or SCD (Fig. 2e) resulting in six different foams (Table S1†). The FD foams (Fig. 2g and Fig. S3†) exhibited a more ordered structure compared to the SCD ones (Fig. 2f and Fig. S3†) resulting in clearly defined honeycomb macropores. The honeycomb structures of the FD foams show a higher resemblance with those of unidirectionally freeze-cast and freeze dried foams prepared from CNFs than those prepared by CNCs, which give honeycomb structures with a higher aspect ratio.[34–36] This suggests that in our CNC–CNF composite foams, the macropore formation is dominated by the entangled CNF network, which restrains the ice crystal growth to a honeycomb morphology even though the CNC loading is high. The CNCs, which do not entangle are expected to decorate and reinforce the CNF network but not contribute to the morphology.[37]

Both the FD and SCD foams possess a hierarchical pore structure consisting of macropores and nanosized pores. The macropores are templated by the unidirectional grown ice crystals during ice-templating while nanosized pore structures are created in the foam walls.[15,22,38] The SCD foams displayed a much larger fraction of nanosized pores (Fig. S4†) and higher BET specific surface area than the FD foams (Fig. 3a and Table S2†). The BET specific surface area ranged between 234–263 $m^2\ g^{-1}$ for the SCD foams and was about 20-fold lower for the FD foams with 6–19 $m^2\ g^{-1}$. A similar trend concerning the specific surface area with respect to the CNC loading and foam density was found by small-angle X-ray scattering (SAXS) experiments. 1D SAXS patterns were fitted with a Porod function to derive a scale factor C which is proportional to the specific surface area (Table S3†). Since the SCD foams displayed a high surface area, their CO_2-uptake *via* physisorption at standard pressure and 273 K was investigated for CNC : CNF-5 : 1_SCD and CNC : CNF-9 : 1_SCD and ranged between 0.379–0.385 mmol g^{-1} (Table S2†). These values lie in the same span as the CO_2 uptake of hydrothermally carbonized chitosan.[39] Although the CO_2-uptake decreased slightly in the following cycles, it stayed around 0.38 mmol g^{-1} for up to four cycles (Fig. S5†). At the same time, all the SCD foams had smaller macropore sizes (8–10 μm) and narrower macropore distribution compared to the FD foams (26–38 μm) (Fig. 3b and Table S2†). High-resolution SEM images of the foam walls confirm the BET surface area and display denser packaging of the nanoparticles in CNC : CNF-5 : 1_FD (Fig. 3c and d) while CNC : CNF-5 : 1_SCD (Fig. 3e and f) showed a much more network-like structures incorporating small pores. The very low BET specific surface area of the FD foams decreased as a function of density. The densely packed foam walls become even more tightly packed with increasing foam density resulting in lower specific surface area.[34] The more network like structure of the SCD foams however behaves differently allowing for more accessible sites with an increase in nanoparticles and therefore a higher surface area with increasing density within the tested density range. It can be speculated that the difference in the foam wall density between the two drying techniques is either caused by local shrinkage and densification during the freeze drying process or by particle-rearrangement in the SCD foams which could appear during the solvent exchange (water–ethanol and/or ethanol–liquid CO_2).

The foams with identical composition that had been prepared by FD and SCD showed differences regarding their structural integrity upon moisture exposure. The FD foams adsorbed slightly more water as a function of RH compared to the SCD foams of the same CNC–CNF ratio (Fig. 4a). The larger macropores allow for easier uptake of water. The effect of the macropore size is in accordance with our previous work on the moisture uptake of freeze dried CNM foams[40] with reduced moisture-uptake for foams with smaller macropores. As a function of foam density and CNC loading, both the FD and the SCD foams show reduced moisture uptake. The cotton CNCs have a much higher crystallinity index than wood CNF, (Fig. S6 and Table S4†) inhibiting the moisture uptake to a certain extent. Our previous work confirmed that the crystalline cellulose is less susceptible to moisture resulting in lower moisture uptake.[40]

The moisture induced shrinkage of the FD and SCD foams was also tested as a function of RH. The SCD foams were significantly more susceptible to shrinking at 80% RH compared to their counterpart FD foams (Fig. 4b). This unexpected behavior indicated that the shrinkage is related to both the composition and the structure. Apparently, the highly ordered honeycomb structure of FD foams is more robust to resist the shrinkage induced by high RH. Additionally, it can be stated that the foams with higher density and higher CNC loading were more resistant to shrinkage, with CNC : CNF-5 : 1_FD and

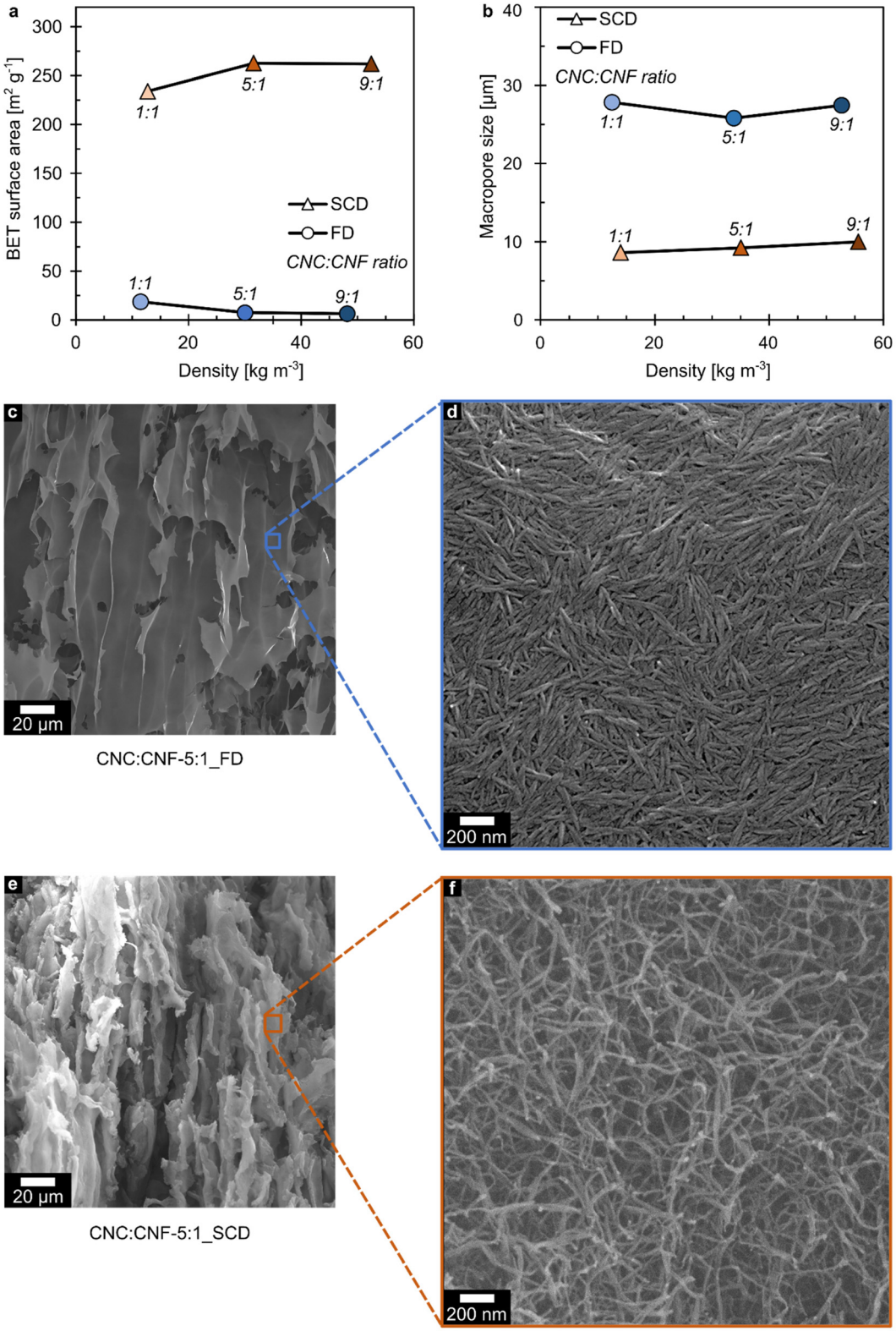

Fig. 3 Pore structure of the FD and SCD anisotropic CNC–CNF foams. (a) BET specific surface area and (b) macropore size of the FD and SCD anisotropic CNC–CNF foams as a function of foam density. SEM image of the foam wall of (c) (d) CNC : CNF-5 : 1_FD and (e) (f) CNC : CNF-5 : 1_SCD foams at different magnifications.

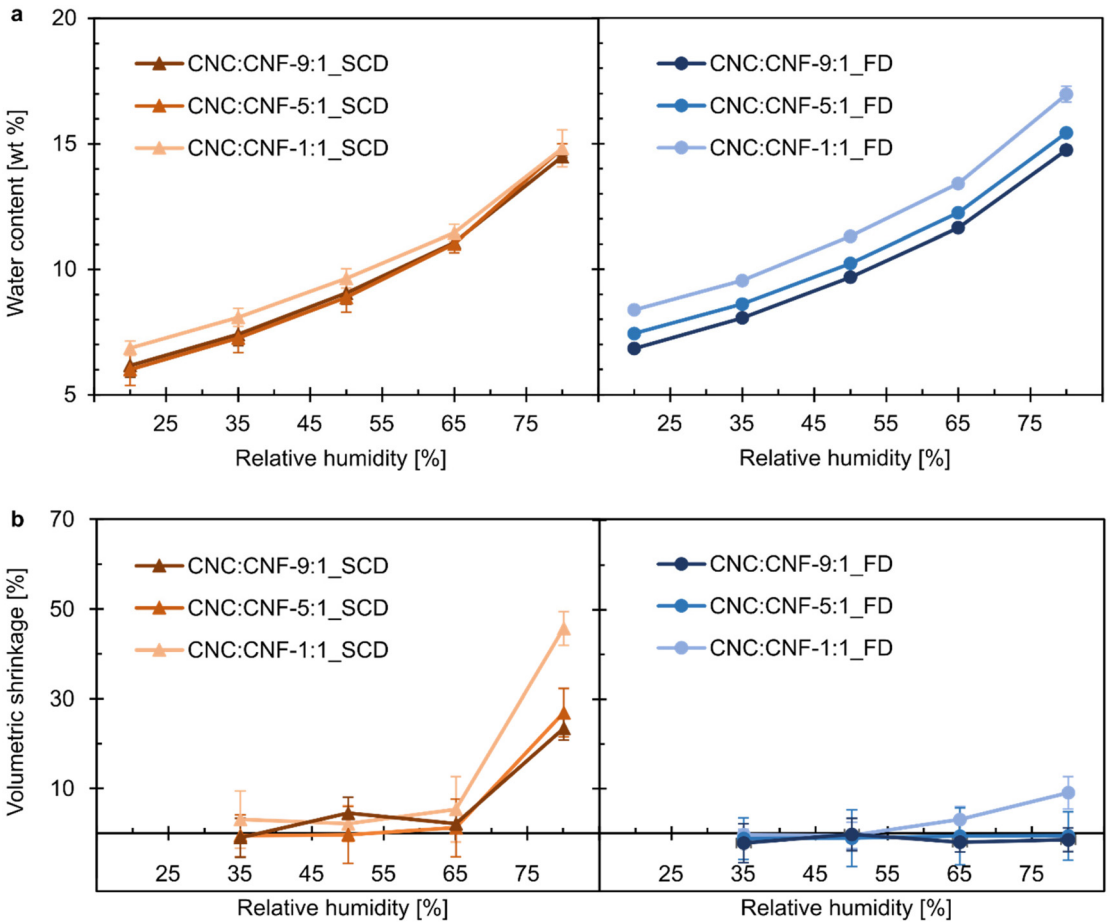

Fig. 4 Moisture resilience of the FD and SCD anisotropic CNC–CNF foams. (a) Moisture uptake of the anisotropic CNC–CNF foams as a function of RH. (b) Volumetric shrinkage of the foams as a function of RH.

CNC : CNF-9 : 1_FD foams showing no significant volume loss up to 80% RH.

Tomographic imaging of CNC : CNF-5 : 1 foam at low (35% RH, Fig. 5a) and high RH (90% RH, Fig. 5b) revealed a swelling and collapse of the SCD foam wall structure at high RH while the more ordered and rigid foam wall structure of the FD foam (Fig. 5c and d) displayed no changes upon moisture exposure. The scale factor C indicated an increase in specific surface area with increasing RH for the SCD foams which might be related to the swelling of the foam walls (Table S3†). 2D patterns of both SAXS and wide-angle X-ray scattering (WAXS) analysis displayed an isotropic particle orientation in the case of the SCD foams (Fig. 5e and f), with the nanoparticles having different rotations angles. In contrast, anisotropic particle orientation was found for the FD foams, which displayed a preferred orientation along the ice-growth direction (Fig. 5g and h). The orientation degree of the FD foams derived from the SAXS 2D patterns ranged between 0.89–0.92 (Fig. 5j), which describes bundles of particles. Furthermore, the orientation degree derived from the WAXS 2D patterns was 0.62–0.71 (Fig. 5k), which describes smaller entities like individual particles. The columnar alignment of the macropores was estimated from SEM images of the foams cut along the axial direction applying the OrientationJ plugin of Fiji. They displayed anisotropic behavior for all types of foams although the anisotropy was lower in the SCD foams compared to the FD foams (Fig. 5i). The general decrease in the orientation degree f with increasing density can possibly be related to the solid-content related change in viscosity of the dispersion which become more gel-like impeding the freeze-casting process. This suggests a hierarchical orientation in the foams with an orientation in the particle level and the columnar macropore level. The lack of orientation in the particle level for the SCD foams matches the network-like structure observed in high-resolution SEM while the alignment of the nanoparticles in the foam wall of the FD sample is reflected in their dense packing.

The thermal conductivity along the radial and axial (Fig. 6a and b) directions were determined using the transient hot disk method. The hot disk technique was validated in regards to the guarded hot disk technique applied on a super-insulating reference material (Fig. S7†).[25,26]

The FD foams displayed a significantly higher thermal anisotropy in comparison to the SCD foams as estimated from

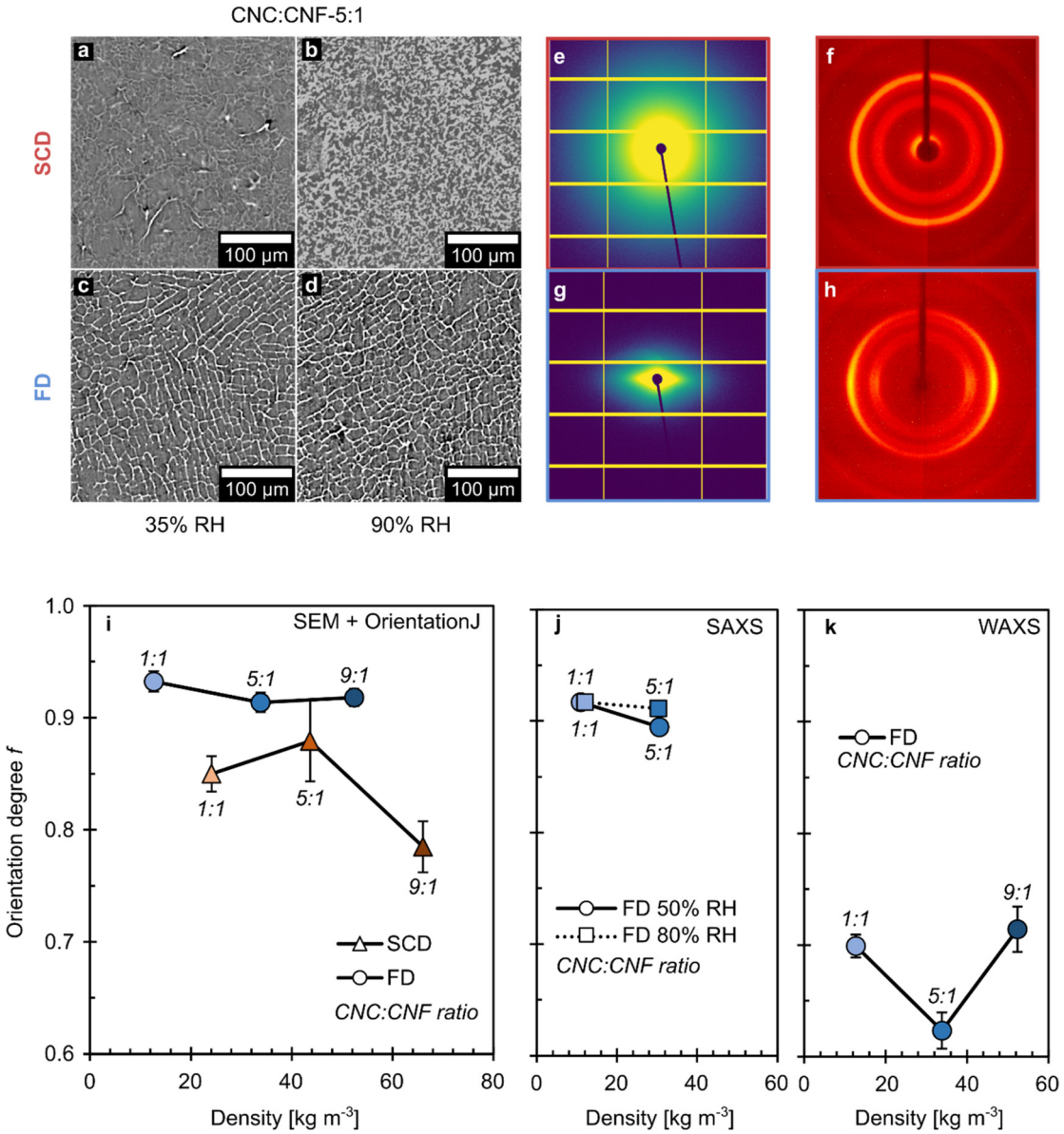

Fig. 5 Nanoparticle and macropore structure and orientation. Tomographic images of the supercritical dried (SCD) CNC : CNF-5 : 1 foams at (a) 35% and (b) 90% RH. Tomographic images of the freeze dried (FD) CNC : CNF-5 : 1 foams at (c) 35% and (d) 90% RH. 2D pattern from (e) small-angle X-ray scattering (SAXS) of CNC : CNF-1 : 1_SCD and (f) wide-angle X-ray scattering (WAXS) of CNC : CNF-5 : 1_SCD. 2D pattern from (g) SAXS of CNC : CNF-1 : 1_FD and (h) WAXS of CNC : CNF-5 : 1_FD. (i) Columnar macropore orientation degree of the foams derived from SEM images along the axial direction applying the Orientation J plugin. (j) particle orientation degree of CNC : CNF-1 : 1_FD and CNC : CNF-5 : 1_FD at 50% RH and 90% RH derived from SAXS (k) particle orientation degree of CNC : CNF-1 : 1_FD, CNC : CNF-5 : 1_FD and CNC : CNF-9 : 1_FD derived from WAXS.

the ratio of the average axial and radial thermal conductivity (Fig. 6c). The high degree of thermal anisotropy of FD foams can be related to the highly aligned CNMs in the columnar foam walls and the macropore orientation. The thermal conductivity of the foams in the radial direction remained around 25–30 mW m^{-1} K^{-1} for densities up to 40 kg m^{-3} and then increased with increasing densities, which is in line with previous studies on anisotropic CNC-based foams.[34] Previous work has related the increase of the radial thermal conductivity with increasing density of the foams with a reduction in interparticle distance that reduces phonon scattering.[9] It is interesting to note that the SCD foams displayed a thermal anisotropy that is around 2 although the nanoparticles in the foams wall are not preferentially aligned in the freezing direction (Fig. 5j and Fig. S8†). The relatively low radial thermal conductivity of the SCD foams may be related to the oriented macropores and to the small pores in the foam walls (Fig. 3f and Fig. S4, Table S2†). The CNC–CNF foams in this study displayed a similar thermal conductivity as freeze dried anisotropic cotton-CNC foams of similar density[18] and a higher

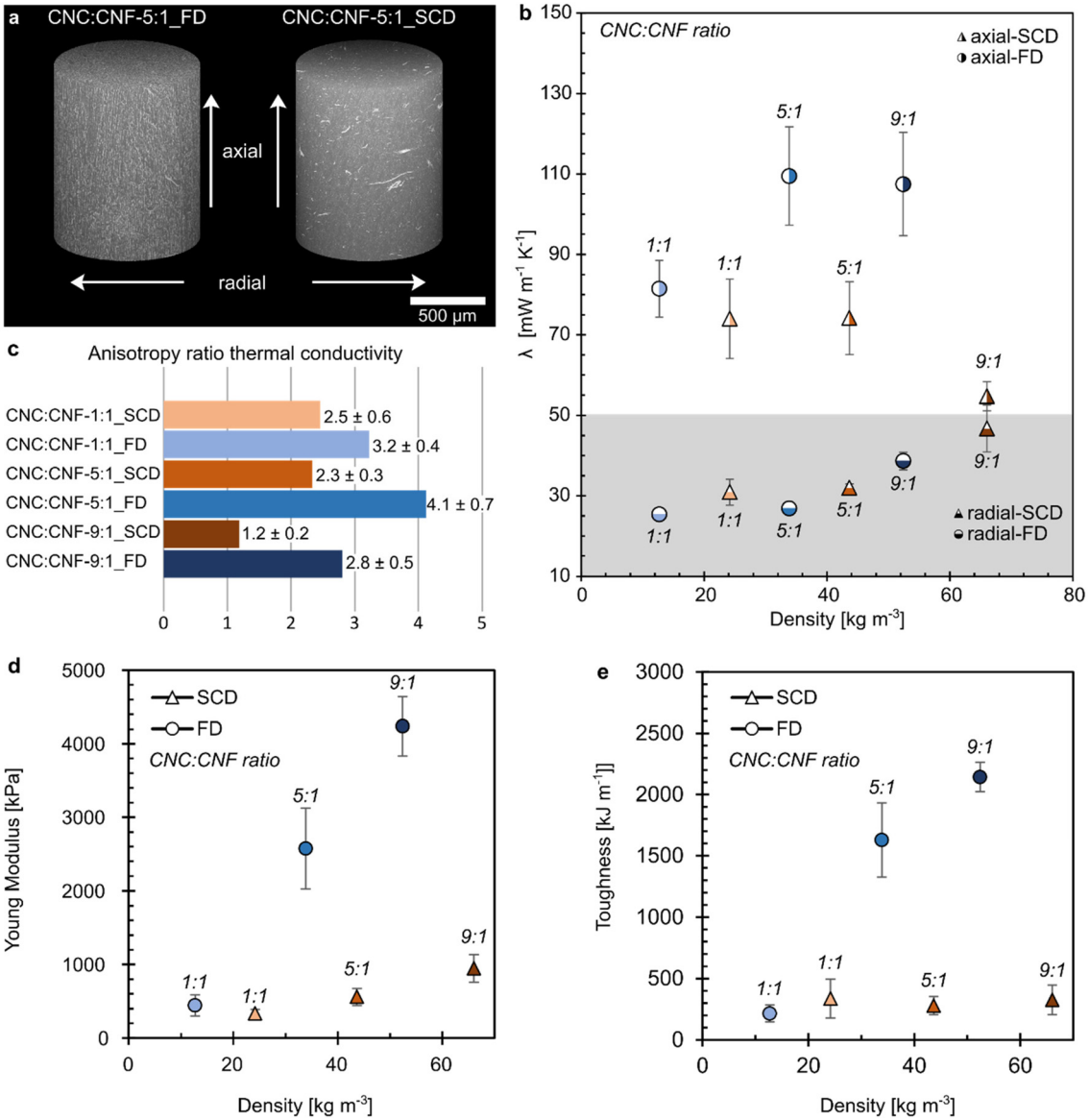

Fig. 6 Thermal insulation and mechanical performance of the FD and SCD anisotropic CNC–CNF foams. (a) Tomographic section (diameter 0.975 mm, height 1.17 mm) images of CNC : CNF-5 : 1_FD (left) and CNC : CNF-5 : 1_SCD (right) foams with indications of the axial and radial direction (b) Thermal conductivity along the axial and radial direction of the FD and SCD anisotropic CNC–CNF foams at 295 K and 50% RH as a function of foam density. (c) Anisotropy ratio (axial/radial) of the thermal conductivity of the CNC–CNF foams (d) Young modulus and (e) toughness along the axial direction of the FD and SCD anisotropic CNC–CNF foams as a function of foam density.

radial thermal conductivity compared to freeze dried anisotropic wood-CNF foams[22,41,42] with a lower foam density. It should be noted that the anisotropic all-cellulose composite foams from post-consumer cotton clothing and wood displayed a radial thermal conductivity similar to commercial fossil-based insulation materials such as polyurethane and polystyrene (20–45 mW m^{-1} K^{-1}).[43–45]

The FD foams showed a higher Young's modulus (Fig. 6d) and a higher toughness (Fig. 6e) than the SCD foams along the axial direction. The better load-bearing properties of the FD foams compared to the SCD foam can be related to the preferential orientation of the nanoparticles in the FD foams that contrasts to the more isotropic organization of the nanoparticles in the SCD foams. The difference was more pronounced for the foams with higher density and a higher share of cotton CNCs. While the specific Young's modulus (Table S6†) of the FD composite foams increased with increasing density from 35 kN m kg^{-1} for CNC : CNF-1 : 1_FD to 81 kN m kg^{-1} for CNC : CNF-9 : 1:FD, the SCD composite foams displayed a low specific Young's modulus of 13–14 kN m kg^{-1} for all compositions. The specific Young's modulus of CNC : CNF-9 : 1:FD is in fact significantly larger than previously reported anisotropic wood-CNC based foams,[36] cotton-CNC based foams[18] and wood-CNF based foams.[46]

Conclusion

We have investigated how the properties of foams prepared from post-consumer cotton CNCs and wood-derived CNFs by unidirectional ice-templating depends on the drying method: freeze drying or supercritical-drying. Nitrogen sorption combined with SEM imaging and X-ray scattering showed that the FD foam walls are composed of tightly packed and aligned nanoparticles while the SCD foams displayed a more open and random network structure with no preferential orientation of the CNMs. The SCD foams had a bigger share (1–3% for SCD *vs.* ≤0.1% for FD) of pores below 300 nm in the foam walls, resulting in at least 12–43 times higher specific surface area than the FD foams. The differences in porosity and particle packing reflected in the moisture resilience, providing the FD foams with lower shrinkage over a wider humidity range in comparison to the SCD foams.

The thermal conductivity in the radial direction was lower than in the axial direction for all foams, irrespective of the density, composition and drying method. The thermal anisotropy was relatively large for the FD foams which was related to the highly aligned CNMs in the foams walls but the SCD foams also displayed a thermal anisotropy around 2 despite the lack of preferential orientation of the nanoparticles. The significantly higher specific Young's modulus and specific toughness in the axial direction of the FD foams compared to the SCD foams could also be related to the preferential axial orientation of the CNMs. Overall, the FD foam with a CNC : CNF ratio of 5 : 1 and a dry density of 34 kg m^{-3} (at 50% RH) combined high Young's modulus (2600 kPa), low radial thermal conductivity, and strong moisture resilience. Its SCD counterpart with a density of 44 kg m^{-3} (50% RH) revealed a high surface area (263 m^2 g^{-1}) and possibilities towards adsorption application and CO_2 uptake (0.38 mmol g^{-1} after 4 cycles).

The identification of the fundamental differences between the FD and SCD foams, despite their identical chemical composition, paves the way to tailor materials suitable for future applications in adsorption, cushioning, packaging, and thermal management. Additionally, it could be shown that cotton clothing derived CNCs can be successfully prepared into lightweight foams, offering a path to repurpose textile waste.

Author contributions

C. S.: conceptualization, investigation, methodology, data curation, visualisation, validation, formal analysis and writing the original and final draft. M.-X. R.-C.: investigation, methodology and review/editing the final draft. T. W.: methodology and review/editing the final draft. E. N. and A. Å.: investigation, methodology, data curation, validation and review/editing the original and final draft. A. P. M.: resources, funding acquisition, review/editing the final draft. G. N.: conceptualization, resources and review/editing the final draft. L. B: conceptualization, resources, funding acquisition and review/editing the original and final draft. V. A.-K: conceptualization, investigation, methodology, data curation, validation, project administration, funding acquisition and writing the original and final draft. All co-authors: writing/review/editing the final draft.

Data availability

The data supporting this article have been included in the main manuscript or as part of the ESI.†

Conflicts of interest

There are no conflicts to declare.

Acknowledgements

The authors acknowledge the financial support from the Stiftelsen Konung Carl XVI Gustafs 50-årsfond för vetenskap, teknik och miljö, 2022, the SSF funded graduate school SwedNess (grant number: SNP21-0004 and GSn15-008) and the Swedish Research Council (grant number: 2023-05572). We also acknowledge support from the Wallenberg Initiative Materials Science for Sustainability (WISE) funded by the Knut and Alice Wallenberg Foundation (KAW). We acknowledge DESY (Hamburg, Germany), a member of the Helmholtz Association HGF, for the provision of experimental facilities. Parts of this research were carried out at PETRA III, and we would like to sincerely thank André Luiz Coelho Conceição for assistance in using P62. Beamtime was allocated for proposal I-20230270 EC.

We acknowledge MAX IV Laboratory for time on Beamline ForMAX under Proposal 20230555, and we would like to sincerely thank, Kim Nygård, Mira Viljanen, Samuel McDonald and Jackson Silva for their support during the measurements.

Research conducted at MAX IV, a Swedish national user facility, is supported by the Swedish Research council under contract 2018-07152, the Swedish Governmental Agency for Innovation Systems under contract 2018-04969, and Formas under contract 2019-02496.

The authors would also like to thank Malwine Lühder for her support during the SAXS and tomography measurements, Emma Berling for the support in foam preparation, Thomas Bergmann for support with supercritical drying as well as Enrico Boschi and Luiz Guilherme Garcia Greca for the guidance and support in the EMPA labs. The Swedish Science Council is gratefully acknowledged for the research infrastructure grant (project number: 2021-00318) for the electron microscopy facilities at Stockholm University and Kjell Jansson is thanked for the help when collecting the high-resolution SEM images.

References

1 E. Niinivaara and E. D. Cranston, *Carbohydr. Polym.*, 2020, **247**, 116664.
2 E. Di Maio, S. Iannace and G. Mensitieri, *Supercritical Fluid Science and Technology*, Elsevier, 2021, vol. 9, pp. 21–32.
3 M.-X. Ruiz-Caldas, V. Apostolopoulou-Kalkavoura and A. P. Mathew, *Cell Rep. Phys. Sci.*, 2024, **5**, 101795.
4 M. X. Ruiz-Caldas, V. Apostolopoulou-Kalkavoura, A. K. Hellström, J. Hildenbrand, M. Larsson, A. Jaworski, J. S. M. Samec, P. Lahtinen, T. Tammelin and A. P. Mathew, *J. Mater. Chem. A*, 2023, **11**, 6854–6868.
5 United States Environmental Protection Agency (EPA), Textiles: Material-Specific Data, **https://www.epa.gov/facts-and-figures-about-materials-waste-and-recycling/textiles-material-specific-data**.
6 V. Apostolopoulou-Kalkavoura, P. Munier and L. Bergström, *Adv. Mater.*, 2020, **2001839**, 1–17.
7 M. Pfundstein, R. Gellert, M. Spitzner and A. Rudolphi, *Insulating Materials*, Institut für internationale Architektur-Dokumentation GmbH & Co. KG, 2008.
8 K. Raed, U. Gross, K. Raed and U. Gross, *Int. J. Thermophys.*, 2009, **30**, 1343–1356.
9 J. A. Diaz, Z. Ye, X. Wu, A. L. Moore, R. J. Moon, A. Martini, D. J. Boday and J. P. Youngblood, *Biomacromolecules*, 2014, **15**, 4096–4101.
10 G. Chen, *Int. J. Therm. Sci.*, 2000, **39**, 471–480.
11 S. Han, J. Hong, Q. Luo, H. Xu, H. Tan, Q. Wang, J. Tao, Y. Zhou, L. Peng, Y. He, J. Shi, N. Ma, Y. Cheng and H. Su, *Atmospheric Chemistry and Physics Discussions*, 2021, pp. 1–25.
12 A. Célino, S. Fréour, F. Jacquemin and P. Casari, *Front. Chem.*, 2014, **1**, 1–12.
13 M. Piggott, *Load Bearing Fibre Composites*, Springer, New York, 2007, vol. 2, pp. 40–65.
14 P. Munier, K. Gordeyeva, L. Bergström and A. B. Fall, *Biomacromolecules*, 2016, **17**, 1875–1881.
15 T. Wu, Z. Zeng, G. Siqueira, K. De France, D. Sivaraman, C. Schreiner, R. Figi, Q. Zhang and G. Nyström, *Nanoscale*, 2020, **12**, 7383–7394.
16 C. Antonini, T. Wu, T. Zimmermann, A. Kherbeche, M.-J. Thoraval, G. Nyström and T. Geiger, *Nanomaterials*, 2019, **9**, 1142.
17 T. Budtova, in *Cellulose Science and Technology: Chemistry, Analysis, and Applications*, 1st edn, 2019, pp. 371–392.
18 M.-X. Ruiz-Caldas, C. Schiele, E. Hadi, M. Andersson, P. Mohammadpour, L. Bergström, A. P. Mathew and V. Apostolopoulou-Kalkavoura, *Carbohydr. Polym.*, 2024, **338**, 122212.
19 S. Groult and T. Budtova, *Carbohydr. Polym.*, 2018, **196**, 73–81.
20 K. Sakai, Y. Kobayashi, T. Saito and A. Isogai, *Sci. Rep.*, 2016, **6**, 20434.
21 O. Korhonen and T. Budtova, *Composites, Part A*, 2020, **137**, 106027.
22 V. Apostolopoulou-Kalkavoura, S. Hu, N. Lavoine, M. Garg, M. Linares, P. Munier, I. Zozoulenko, J. Shiomi and L. Bergström, *Matter*, 2021, **4**, 276–289.
23 K. Kriechbaum, P. Munier, V. Apostolopoulou-Kalkavoura and N. Lavoine, *ACS Sustainable Chem. Eng.*, 2018, **6**, 11959–11967.
24 V. Apostolopoulou-Kalkavoura, K. Gordeyeva, N. Lavoine and L. Bergström, *Cellulose*, 2018, **25**, 1117–1126.
25 Center of Applied Energy Research, Reference Materials, **https://en.cae-zerocarbon.de/Thermal-Reference-Material.html**, (accessed 16 April 2024).
26 H.-P. Ebert, S. Braxmeier, G. Reichenauer, F. Hemberger, F. Lied, D. Weinrich and M. Fricke, *Int. J. Thermophys.*, 2021, **42**, 21.
27 L. A. Feigin and D. I. Svergun, *Structure Analysis by Small-Angle X-Ray and Neutron Scattering*, Plenum Press, New York, 1987.
28 G. Porod, *Kolloid-Z.*, 1951, **124**, 83–114.
29 SasView, Porod function, **https://www.sasview.org/docs/old_docs/4.1.2/user/models/porod.html**, (accessed 16 April 2024).
30 Z. Wang, Z. Yao, J. Zhou and Y. Zhang, *Carbohydr. Polym.*, 2017, **157**, 945–952.
31 Y. Okita, T. Saito and A. Isogai, *Biomacromolecules*, 2010, **11**, 1696–1700.
32 K. Daicho, K. Kobayashi, S. Fujisawa and T. Saito, *Biomacromolecules*, 2020, **21**, 939–945.
33 T. V. Bommaraju, *Water Qual. Res. J.*, 1995, **30**, 339–361.
34 V. Apostolopoulou-Kalkavoura, P. Munier, L. Dlugozima, V.-L. Heuthe and L. Bergström, *Sci. Rep.*, 2021, **11**, 18685.
35 P. Munier, K. Gordeyeva, L. Bergström and A. B. Fall, *Biomacromolecules*, 2016, **17**, 1875–1881.
36 C. Schiele, A. Di, S. E. Hadi, P. K. B. Rangaiah, R. Augustine and L. Bergström, *Adv. Mater. Interfaces*, 2024, **11**, 2300996.
37 S. Gupta, F. Martoïa, L. Orgéas and P. J. J. Dumont, *Appl. Sci.*, 2018, **8**, 2463.
38 B. Wicklein, A. Kocjan, G. Salazar-Alvarez, F. Carosio, G. Camino, M. Antonietti and L. Bergström, *Nat. Nanotechnol.*, 2015, **10**, 277–283.
39 J. A. O. Chagas, G. O. Crispim, B. P. Pinto, R. A. S. San Gil and C. J. A. Mota, *ACS Omega*, 2020, **5**, 29520–29529.
40 M. Garg, V. Apostolopoulou-Kalkavoura, M. Linares, T. Kaldéus, E. Malmström, L. Bergström and I. Zozoulenko, *Cellulose*, 2021, **28**, 9007–9021.
41 A. Di, C. Schiele, S. E. Hadi and L. Bergström, *Adv. Mater.*, 2023, **35**, 2305195.
42 K. Kriechbaum, V. Apostolopoulou-Kalkavoura, P. Munier and L. Bergström, *ACS Sustainable Chem. Eng.*, 2020, **8**, 17408–17416.
43 B. Petter Jelle, *Energy Build.*, 2011, **43**, 2549–2563.
44 M. Jerman and R. Černý, *Energy Build.*, 2012, **53**, 39–46.
45 U. Jarfelt, O. Ramnäs, U. Jarfelt and O. Ramnäs, 0th International Symposium on District Heating and Cooling Sektion 6 a Heat distribution-pipe properties Thermal conductivity of polyurethane foam Best performance.
46 P. Munier, V. Apostolopoulou-Kalkavoura, M. Persson and L. Bergström, *Cellulose*, 2020, **27**, 10825–10836.